

Topological Transitions in two-dimensional Floquet superconductors

Paul Wenk,^{1,*} Milena Grifoni,² and John Schliemann²

¹*Institute for Physical Chemistry, University of Münster, Münster, Germany*

²*Institute for Theoretical Physics, University of Regensburg, Regensburg, Germany*

(Dated: October 17, 2022)

We demonstrate the occurrence of a topological phase transition induced by an effective magnetic field in a two-dimensional electron gas with spin-orbit coupling and in proximity to an s -wave superconductor. The effective, perpendicular magnetic field is generated by an in plane, off-resonant ac-magnetic field or by circularly polarized light. The conditions for entering the topological phase do not rely on fine parameter tuning: For fixed frequency, one requires a minimal amplitude of the effective field which can be evaluated analytically. In this phase, chiral edge states generally emerge for a system in stripe geometry unless the Rashba and Dresselhaus coupling have the same magnitude. In this special case, for magnetic field driving the edge states become Majorana flat bands, due to the presence of a chiral symmetry; the light irradiated system is a trivial superconductor.

I. INTRODUCTION

Nowadays pathways to manipulate material properties by a time-periodic drive are often dubbed as “Floquet engineering”¹. This is based on the observation that the time evolution and steady state of a quantum system under time-periodic driving can be described in terms of a Floquet Hamiltonian, whose quasi-eigenenergy spectrum can be entirely different from the spectrum of the undriven Hamiltonian^{2,3}. The growing interest in this field is fueled by rapid developments in optical and microwave coherent control techniques, together with the possibility of engineering novel quantum materials exhibiting exotic electronic properties. For example time- and angle-resolved photoemission spectroscopy⁴ has been used to image the Floquet-Bloch surface states of a topological insulator, and to demonstrate that the surface Dirac cone becomes gapped upon irradiation by circularly polarized light⁵. Vice versa, intense circularly polarized light might turn a trivial static conductor like graphene into a Haldane’s Chern insulator supporting chiral edge modes⁶.

While Floquet topological insulators are by now largely understood, the study of Floquet topological superconductors, in the focus of this work, is still in an early stage. *Static* topological superconductors have attracted a great deal of interest for the realization of Majorana fermions in solid states and their possible application to topological quantum computation⁷. Crucially, the target system should have spin nondegenerate bands, e.g. due to the combined effects of spin-orbit coupling (SOC) and of a magnetic field. The possibility of tuning topological superconductivity by light has been discussed by now in various one-dimensional setups ranging from cold atom chains to Rashba nanowires^{8–13}. Some studies have addressed the possibility to observe Floquet-Majorana modes in finite two-dimensional (2D) systems, like the Kitaev model on honeycomb lattices¹⁴, a two-band model with s -wave pairing on a square lattice¹⁵, or a square model with d -wave pairing for cuprate superconductivity¹⁶. By applying off-resonant drive modulating some of the system’s properties (chemical potential, spin-orbit

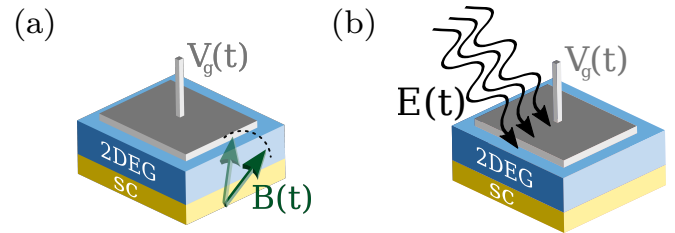


Figure 1. A 2DEG in proximity to a conventional superconductor can become itself a (synthetic) superconductor. The combined action of spin-orbit coupling (SOC) and a time-dependent magnetic (a) or electric (b) field can drive the system to a topologically non trivial phase.

coupling strength, etc.), edge modes have been predicted based on numerical diagonalization of the associated Floquet Hamiltonians. In a recent work, Plekhanov *et al.*¹⁷ have posed the question, whether a Floquet topological phase transition can be entered also in the more conventional set-up of a two-dimensional electron gas (2DEG) with spin-orbit coupling being proximity coupled to an s -wave superconductor. Under resonance conditions between two spin-orbit split bands, an out-of plane magnetic field, see Fig. 1(a), is predicted to induce helical edge modes. Despite appealing, a limitation of this proposal is that the resonant condition can be satisfied only in a restricted region in k -space. Where the resonance is not satisfied, more and more Floquet subbands participate in the low energy behavior and the topological gap disappears.

Motivated by the former studies on 2D Floquet superconductors^{15–17}, we investigate here the impact of off-resonant time-dependent electromagnetic fields for the setups in Fig. 1. Although we prevalently focus on the one in Fig. 1(a), the two-models map onto similar effective Hamiltonians obtained by using Löwdin partitioning. We find that a high-frequency in plane ac-magnetic field generates an out-of plane component of an effective static magnetic field which can drive the topological phase transition. Our analytical results are corroborated by diagonalization of the full Floquet Hamiltonian for bulk as well

as stripe geometries. The topological phase boundaries can be calculated analytically, and are well in agreement with numerical predictions for topological invariants of the bulk system. In turn, the Floquet spectrum of a finite stripe displays chiral edge modes crossing at the Γ point, for generic values of the SOC, in the parameter region of finite Chern number. Remarkably, flat bands are found in the limit of equal amplitude but different sign of Rashba and Dresselhaus SOC. They are enforced by a chiral symmetry of the driven system¹⁸ present in this special case. For the laser irradiated setup, the effective out-of-plane magnetic field vanishes when the Rashba and Dresselhaus SOC have the same amplitude. In this case there is no topological phase. Finally, an interesting scaling of the topological phase transition with system size is observed.

The paper is structured as follows: In Sec. II we construct the Floquet-Bogoliubov de Gennes (BdG) Hamiltonian matrix for our model, while in Sec. III the high frequency effective Hamiltonian is derived within Löwdin perturbation theory^{19,20}. In Sec. IV numerical results are presented for stripe geometries and compared with the expectation of the effective static model. Finally, conclusions are drawn in Sec. V. Details of the calculations are presented in Appendices A–C.

II. MODEL

With focus on the setup of Fig. 1(a) we consider a continuum Hamiltonian near the Γ point

$$\mathcal{H}(t) = \mathcal{H}_0 + \mathcal{H}_\Delta + \mathcal{H}_1(t), \quad (1)$$

where the static part describes a 2DEG with Rashba^{21,22} (α) and linear Dresselhaus²³ (β) SOC in proximity to an s -wave superconductor. Explicitly,

$$\begin{aligned} \mathcal{H}_0 = & \sum_{\sigma\sigma'} \int d^2k \psi_{\mathbf{k}\sigma}^\dagger \left(\frac{\hbar^2 k^2}{2m^*} - \mu - \alpha_x k_x \sigma_y + \alpha_y k_y \sigma_x \right) \psi_{\mathbf{k}\sigma'}, \\ \mathcal{H}_\Delta = & -\frac{\Delta}{2} \sum_{\sigma\sigma'} \int d^2k \left(\psi_{\mathbf{k}\sigma}^\dagger (i\sigma_y)_{\sigma\sigma'} \psi_{-\mathbf{k}\sigma'}^\dagger + \text{h.c.} \right). \end{aligned} \quad (2)$$

Here, $\psi_{\mathbf{k}\sigma}^\dagger$ ($\psi_{\mathbf{k}\sigma}$) are creation (annihilation) operators of an electron with spin component σ along the z direction and wave vector \mathbf{k} ; for the SOC constants we define $\alpha_x := \alpha + \beta$, $\alpha_y := \alpha - \beta$, and in real as well as spin space the x -coordinate axis points along the crystallographic $[1, \bar{1}, 0]$ -direction while the y -axis lies along $[1, 1, 0]$; m^* is the effective mass and μ the chemical potential. Superconductivity induced in the 2DEG by proximity effects is captured by the mean-field Hamiltonian \mathcal{H}_Δ , where Δ is the proximity induced superconducting gap. For the time-dependent part driving the spin dynamics in the 2DEG we consider the generic expression

$$\mathcal{H}_1(t) = \sum_{\sigma\sigma'} \int d^2k \psi_{\mathbf{k}\sigma}^\dagger (\mathbf{A}(t) \cdot \boldsymbol{\sigma})_{\sigma\sigma'} \psi_{\mathbf{k}\sigma'}. \quad (3)$$

Here, $A_i(t) = \mu_B (g_i/2) B_i(t)$, with g_i the effective gyromagnetic ratio along the i -direction, the magnetic field amplitude

$$B_i(t) = B_{ic} \cos(\Omega t) + B_{is} \sin(\Omega t), \quad (4)$$

$\boldsymbol{\sigma} = (\sigma_x, \sigma_y, \sigma_z)$ the vector of Pauli matrices. Thus, in full generality,

$$\mathbf{A}(t) = \mathbf{q} \cos(\Omega t) + \mathbf{r} \sin(\Omega t) \quad \text{with} \quad \mathbf{q}, \mathbf{r} \in \mathbb{R}^3. \quad (5)$$

Due to the periodicity of the external magnetic field, we use Floquet theory to find the quasi-energy spectrum and discuss topological properties. Explicitly, the time dependent problem can be recast onto an effective static problem for the Floquet Hamiltonian

$$\mathcal{H}_F(t) = \mathcal{H}(t) - i\hbar \partial_t \quad (6)$$

when working in the composite Sambe space $\mathcal{S} = \mathbb{T} \otimes \mathbb{H}$ spanned by time periodic functions and the conventional Hilbert space \mathbb{H} ^{1,3}. We introduce the matrix elements in \mathbb{T} of $\mathcal{H}(t)$ in terms of the Fourier transform

$$\mathcal{H}_{mn} = (m|\mathcal{H}(t)|n) := \frac{1}{T} \int_0^T dt \mathcal{H}(t) e^{i(m-n)\Omega t}. \quad (7)$$

In turn the Floquet Hamiltonian has matrix elements

$$(\mathcal{H}_F)_{mn} := \mathcal{H}_{mn} - n\hbar\Omega\delta_{mn}. \quad (8)$$

Diagonalization of \mathcal{H}_F then yields the quasienergy spectrum of the driven system. Care has to be taken when including the contribution of the mean field term \mathcal{H}_Δ in Eq. (7). Due to the presence of two creation or two annihilation operators, the superconducting term is off-diagonal in Sambe space and couples Fourier modes n and $-n$.

Similar to the case of static superconductors, the evaluation of the quasi-energy spectrum is more conveniently performed introducing the Nambu spinor $\Psi_{\mathbf{k}}^\dagger = (\psi_{\mathbf{k}\uparrow}^\dagger, \psi_{\mathbf{k}\downarrow}^\dagger, \psi_{-\mathbf{k}\uparrow}, \psi_{-\mathbf{k}\downarrow})$. Then $\mathcal{H}(t)$ can be expressed in terms of BdG matrices,

$$\mathcal{H}(t) = \frac{1}{2} \int d^2k \Psi_{\mathbf{k}}^\dagger (H_0(\mathbf{k}) + H_\Delta + H_1(t)) \Psi_{\mathbf{k}}. \quad (9)$$

The three parts of the BdG Hamiltonian are given by²⁴

$$\begin{aligned} H_0 &= (\varepsilon_{\mathbf{k}} - \mu) \tau_z \otimes \mathbb{1}_2 + \alpha_y k_y \mathbb{1}_2 \otimes \sigma_x - \alpha_x k_x \tau_z \otimes \sigma_y, \\ H_\Delta &= \Delta \tau_y \otimes \sigma_y, \\ H_1(t) &= A_z(t) \tau_z \otimes \sigma_z + A_x(t) \tau_z \otimes \sigma_x + A_y(t) \mathbb{1}_2 \otimes \sigma_y, \end{aligned} \quad (10)$$

with $\varepsilon_{\mathbf{k}} = \hbar^2 k^2 / 2m^*$ and τ_i Pauli matrices in Nambu space. Together with Eq. (7), this leads to the Floquet-BdG matrix

$$(\mathcal{H}_F)_{mn} := H_{mn} - n\hbar\Omega\delta_{mn}\tau_z \otimes \mathbb{1}_2. \quad (11)$$

Diagonalization of \mathcal{H}_F then yields the quasienergy spectrum of the driven system. Its form is provided in Appendix A. While for generic driving frequencies a numerical diagonalization is required, analytical results can be obtained for off-resonant driving, the case of interest in this work.

III. HIGH-FREQUENCY LIMIT: LÖWDIN PARTITIONING

High-frequency driving is known to be an excellent tool to dress parameters of the static, unperturbed Hamiltonian, e.g. hopping elements or on-site energies²⁵, leading to phenomena like coherent destruction of tunneling or dynamical localization³, which can be used to steer a topological phase transition²⁶. In addition, off-resonant drive can generate terms absent in the static Hamiltonian¹⁶, a crucial effect in the following. Starting from the Floquet matrix $(H_F)_{mn}$, we truncate it by retaining only the $\{m, n = 0, \pm 1\}$ blocks (of dimension 4×4) into account. This gives rise to three Floquet modes. The truncation is justified when $W/\hbar\Omega$ is a small quantity, with W being the static bandwidth. We then apply the Löwdin perturbation scheme^{19,20}, allowing us to fold the effects of terms including the higher harmonics ± 1 in an effective static model with only the $n = 0$ block. Explicitly, see Appendix A 2, Löwdin perturbation up to first order in $W/\hbar\Omega$ results in the effective BdG Hamiltonian

$$H_{\text{eff}} = H_0 + H_\Delta + \frac{\Lambda_z}{\hbar\Omega} \tau_z \otimes \sigma_z + \frac{\Lambda_y}{\hbar\Omega} \mathbb{1}_2 \otimes \sigma_y + \frac{\Lambda_x}{\hbar\Omega} \tau_z \otimes \sigma_x \quad (12)$$

with $\mathbf{\Lambda} = \mathbf{r} \times \mathbf{q}$. Notably, the *in plane* components of the magnetic field generate an *out of plane* term in the effective Hamiltonian. This feature is crucial for the occurrence of the topological phase transition. Hence, in the following we choose $B_z = 0$, such that $\Lambda_x = \Lambda_y = 0$. Introducing the Zeeman term $h_Z := \Lambda_z/\hbar\Omega$, the effective BdG Hamiltonian reduces to the appealing form

$$H_{\text{eff},Z} = (\varepsilon_k - \mu) \tau_z \otimes \mathbb{1}_2 - \alpha_x k_x \tau_z \otimes \sigma_y + \alpha_y k_y \mathbb{1}_2 \otimes \sigma_x + \Delta \tau_y \otimes \sigma_y + h_Z \tau_z \otimes \sigma_z. \quad (13)$$

The spectrum of $H_{\text{eff},Z}$ can be evaluated in closed form. Importantly, the superconducting term exhibits a *p*-wave component in the eigenbasis of the normal conducting ($\Delta = 0$) system, see Appendix A. The gap closing condition yields the critical Zeeman amplitude $h_{Z,c}$ which separates the topologically trivial from the non-trivial phase. For $|\alpha| \neq |\beta|$ it is

$$|h_{Z,c}| = \sqrt{\Delta^2 + \mu^2}. \quad (14)$$

This result is remarkably simple, independent of the SOC strength, and closely resembles the one for some Rashba 1D²⁷ and 2D²⁸ setups. It implies that chiral edge modes should appear in a finite size system, under appropriate choice of the system's parameters.

IV. EDGE MODES IN STRIPE GEOMETRIES

The emergence of such chiral modes is confirmed from a numerical evaluation of the quasi-energy spectrum of

the Floquet-BdG Hamiltonian H_F in stripe geometry. Further, topological invariants for the bulk system were calculated numerically and also agree with the expectations of the simple high frequency model. The numerical results can be seen in Figs. 2–4, and are commented in detail below.

A. $|\alpha| \neq |\beta|$, chiral edge modes

For generic values of the spin-orbit coupling parameters α and β chiral modes are expected to emerge in the topological phase. This is observed in Figs. 2(a) and 2(b). Further, Fig. 2(c) demonstrates the exponential decay of the modes towards the interior of the stripe. The prediction of a topological boundary given in Appendix A 3 by Eq. (14) [red line in Fig. 2(d)] agrees with a numerical evaluation of the Chern numbers C_α ^{29–31} associated to the four quasienergy bands $\varepsilon_{\mathbf{k}\alpha}$, $\alpha = 1, 2, 3, 4$ of the central Floquet zone of the bulk Floquet Hamiltonian H_F (see Appendix B). As seen in Fig. 2(d), $C_2 = 0, 1$ before and after the gap closing at $h_{Z,c}$. Because the phase boundary only depends on the ratio h_Z/Δ and μ/Δ , it does not change if these quantities are scaled by the same factor. For the edge modes to appear though the width of the system should be appropriately changed, such that the decay lengths of the modes remains much smaller than the width. This property can be verified from the figures shown in the Appendix. Here, the relevant scales are a factor 20 larger; edge modes appear for correspondingly narrower stripes.

B. $|\alpha| = |\beta|$, Majorana flat bands

The above results are quite generic and hold true for off-resonant driving and $|\alpha| \neq |\beta|$. Hence they do not require fine tuning of parameters. In the following we discuss one of the special symmetry settings supporting persistent spin helices^{32–35}, $|\alpha| = |\beta|$. Here, a special choice of parameters leads to Majorana flat bands³⁶. This can occur in two situations. In case I the Rashba and Dresselhaus SOC strength have opposite sign $\alpha = -\beta$, which implies $\alpha_x = 0$, and $\alpha_y = 2\alpha$. Then, Majorana flat bands are found in stripe geometry with finite width along the *y*-direction. In the case II, $\alpha = \beta$, the flat bands occur for a finite width of the stripe in the *x*-direction. We demonstrate below that the emergence of flat bands is strictly related to the presence of an additional chiral symmetry of the driven system.

A magnetic field breaks time-reversal symmetry. Hence, for a generic parameter set, also the effective BdG Hamiltonian Eq. (13) is only invariant under particle-hole symmetry, with $\mathcal{P} = \tau_x \otimes \mathbb{1}_2 \mathcal{K}$ the associated antiunitary particle-hole operator and \mathcal{K} the operator of complex conjugation; it holds $\mathcal{P}^2 = 1$. In this case the system belongs in 2D to the symmetry class D³⁷, and its topological properties are well described in terms of Chern numbers, as discussed above. For the special case I,

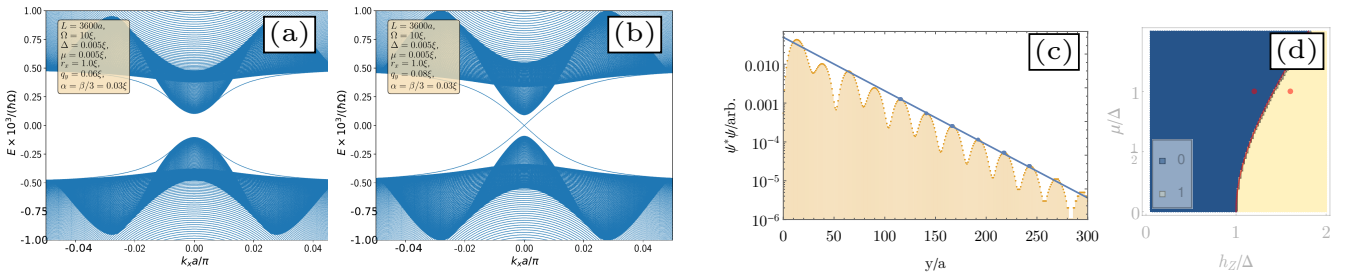


Figure 2. Topological phase transition induced by an in plane time-dependent magnetic field. (a)-(b) Numerical quasienergy spectrum of H_F in stripe geometry for the two values of chemical potential and Zeeman field shown with red dots in panel (d). We considered $N_y = 3600$ transverse channels and retained $N_F = 3$ Floquet modes. In the topological phase, panel (b), chiral mode crossing at the Γ point emerge. (c) The two chiral edge modes decay exponentially towards the device interior and are localized at opposite edges. Here one of them is shown for $k_x a = 0.1$. (d) Chern number C_2 of the bulk Floquet-BdG Hamiltonian for different values of h_Z and μ . It holds $C_2 = 1$ in the nontrivial region; its boundary, depicted by the red solid line, is given by Eq. (14).

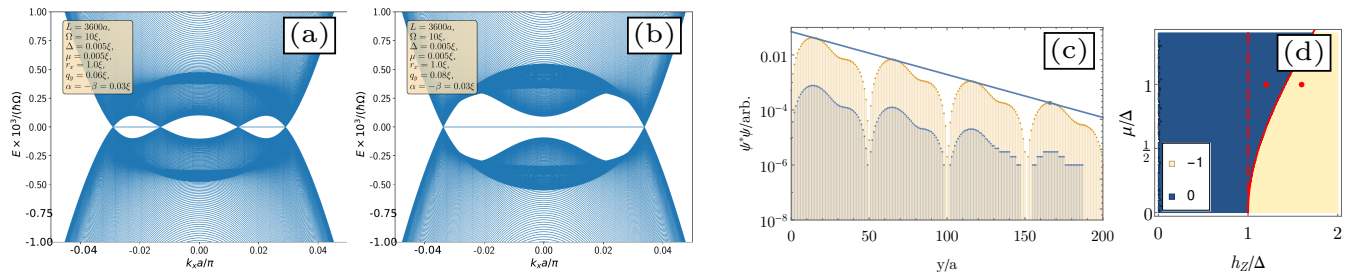


Figure 3. Majorana flat bands for the symmetric case with SOC parameters $\alpha = -\beta$. (a)-(b) Quasienergy spectrum of H_F in stripe geometry with Zeeman amplitude and chemical potential corresponding to the two red dots on the left (a) and right (b) of the topological phase boundary [solid red line in panel (d)]. (c) The spatial profile of the Majorana modes is shown for $k_x a = 0.1$. (d) The Partial Berry-phase sum parity $P_{B,k_x=0} = P_{B,k_x=\pi/2}$ is shown as a function of h_Z/Δ and μ/Δ . The dashed vertical line separates the region with and without flat bands.

$\alpha = -\beta$, the effective Hamiltonian acquires a chiral symmetry with $\mathcal{C}_I = \tau_y \otimes \sigma_z$ the associated unitary operator obeying $\mathcal{C}_I^2 = 1$. As a consequence, the high frequency BdG Hamiltonian is also invariant under the time-reversal operation generated by $\mathcal{T}_I = \mathcal{P}\mathcal{C}_I$. Notice that $\mathcal{T}_I^2 = -1$. In this case the system belongs to the symmetry class DIII; it can support flat bands if the associated \mathbb{Z}_2 invariant becomes nontrivial⁷. Similarly, we find for case II, $\alpha = \beta$, the chiral symmetry $\mathcal{C}_{II} = \tau_x \otimes \mathbb{1}_2$. The gap can now close at finite momenta. Introducing polar coordinates $k_x = k \cos \theta$, $k_y = k \sin \theta$, the closing occur when $\theta = 0, \pi/2$ for case I, II respectively, and

$$|h_{Z,c}(k)| = \sqrt{\Delta^2 + (\mu - a^2 k^2 \xi)^2}, \quad (15)$$

where ξ is the hopping energy and a the lattice constant in the square lattice tight-binding formulation. In Fig. 3 the appearance of flat bands hosting Majorana edge modes is shown for case I and a stripe with finite width along the y -direction. Notice that only the amplitude of the spin-orbit coupling strength was changed compared to Fig. 2. Also, no flat bands are found in case II. The situation is reverted if the stripe has a finite geometry

along the x -direction, reflecting the directionality of the effective SOC field. According to Eq. (15), see Fig. 3(a), situations may happen where flat bands only exist in certain regions of k -space. This mixed regime occurs in the parameter region between the topological phase boundary and the vertical red line in Fig. 3(d). We expect the mini-flat bands not to be stable against perturbations. Here, as \mathbb{Z}_2 invariant the partial Berry phase numbers proposed in Ref. [18] were used, see Sec. C4 of the Appendix.

C. Topological signatures beyond off-resonance

The topological phase transition and the associated edge modes in finite geometries have been obtained for driving energies $\hbar\Omega$ much larger than the bandwidth W of the static 2D system. In Fig. 4 we show that topological features are clearly discerned also for $\hbar\Omega = 7\xi$, where ξ is the hopping energy in the tight-binding formulation. A series of crossing and avoided crossing is observed not

only for the in gap modes, but also for the higher energy. Such features are common to other topological systems and are a signature of the topological character of the excitations near the avoided crossing, see, e.g., Refs. [38 and 39].

V. EXPERIMENTAL FEASIBILITY AND CONCLUSIONS

We have demonstrated the emergence of topologically non-trivial phases in a theoretical model of a 2DEG subjected to an in plane off-resonant magnetic field. A natural question is to which extent such phases can be observed in the state of the art experimental set-ups. For a 2DEG from ordinary III-V semiconductors we estimate a hopping $\xi \simeq 1.5$ eV, which implies frequencies in the energy range $\hbar\Omega = 5 - 15$ eV for the plots in Figs. 2 – 4. Further, with $\Delta \simeq 0.1$ meV and a gyromagnetic ratio $g = 50$ (e.g. for InSb⁴⁰), one finds magnetic field amplitudes $B_{xs} \simeq B_{yc} \approx 30$ T. These are rather large and destroy superconductivity, if the latter is induced through proximity to a conventional superconductor like Nb having critical fields in the order of 0.8 T. A possible extension of this work thus points to proximity to 2D Ising superconductors, like e.g. NbSe₂, which are known to support large in plane critical fields of more than 30 T⁴¹. Signatures of triplet superconductivity were recently observed in trilayer NbSe₂ driven by a static in plane magnetic field up to 33 T⁴². The pairing function discussed there has similar *s*- and *p*-wave components as derived in Appendix A. This suggests related low-energy physics for seemingly distinct 2D superconductors. Alternating magnetic fields with amplitudes of several Tesla are also difficult to achieve in ordinary laboratories. Hence, we would like to comment also on the setup in Fig. 1(b), with the 2DEG driven by circularly polarized light with vector potential $\mathcal{A}(t) = (\mathcal{A} \cos(\Omega t), \mathcal{A} \sin(\Omega t), 0)$. In this case, the light couples to the 2DEG electrons through a minimal coupling $\mathbf{k} \rightarrow \mathbf{k} - \mathbf{k}_0(t)$, with $\mathbf{k}_0(t) = (e/c\hbar)\mathcal{A}(t)$. Following Refs. [16 and 43], in the off-resonant case, Löwdin perturbation theory leads again to the Hamiltonian Eq. (13), with the replacement $m^* \rightarrow m^*/J_0(x)$, $\alpha_{x,y} \rightarrow \alpha_{x,y}J_0(x)$ in the single particle part and $\Lambda_z \rightarrow -(\alpha_x\alpha_y/a^2)J_1^2(x)$. Here, $J_n(x)$ is a Bessel function of first kind and $x = (ea/c\hbar)\mathcal{A}$. Driving by light has the advantage that, since $|J_0| \leq 1$, the hopping $\xi \simeq 1/m^*$ gets effectively reduced and hence also the frequencies Ω being required. Also for this model chiral modes are expected for effective magnetic fields h_Z larger than the critical field Eq. (14) and generic SOC parameters. However, in the symmetric cases $\alpha = \pm\beta$ is either $\alpha_x = 0$ or $\alpha_y = 0$, leading to a vanishing h_Z and thus to trivial superconductivity. In summary, in our work we focused on proximitized semiconducting 2DEGs with strong spin-orbit coupling as possible systems for the realization of a Floquet topological superconductor. However, the large amplitudes

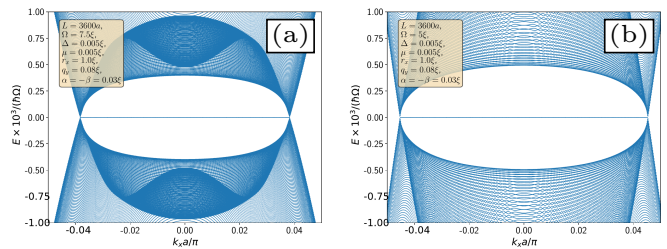


Figure 4. Stability of flat bands. Midgap states and Majorana oscillations are still seen by lowering the driving frequency from $\hbar\Omega = 7.5 \xi$ in panel (a) to $\hbar\Omega = 5 \xi$ in panel (b).

of the magnetic/electric fields and the high frequencies necessary to induce Floquet topological superconductivity indicate the need to look for alternative 2D materials. We suggest that 2D superconductors of the Ising type, like few layers NbSe₂, are an ideal candidate to observe the topological phase transition. Since off-resonant magnetic fields induce effective static magnetic fields, our analysis can be applied also to situations in which only appropriate static fields are applied.

ACKNOWLEDGMENTS

This work was supported by the German Science Foundation under CRC 1277, Project No. B09. We thank J. Klinovaja and D. Loss for discussions.

Appendix A: Floquet BdG Hamiltonian in the continuum model

1. BdG Hamiltonian in Sambe space

We explicitly derive the Floquet-BdG matrix associated to the continuum model Hamiltonian

$$\mathcal{H}(t) = \mathcal{H}_0 + \mathcal{H}_\Delta + \mathcal{H}_1(t), \quad (\text{A1})$$

defined in Eq. (1). Since $\mathcal{H}(t)$ is time periodic, $\mathcal{H}(t) = \mathcal{H}(t + T)$, with the driving period $T = 2\pi/\Omega$, we can apply Floquet theory^{3,44}. The solution to the Schrödinger equation

$$i\hbar\partial_t |\phi_\alpha(t)\rangle = \mathcal{H}(t) |\phi_\alpha(t)\rangle \quad (\text{A2})$$

are Floquet states

$$|\phi_\alpha(t)\rangle = e^{\frac{i}{\hbar}\epsilon_\alpha t} |u_\alpha(t)\rangle, \quad (\text{A3})$$

with the quasienergies ϵ_α and the Floquet functions $|u_\alpha(t)\rangle$. The latter are eigenstates of the Floquet Hamiltonian $\mathcal{H}_F(t) := \mathcal{H}(t) - i\hbar\partial_t$,

$$\mathcal{H}_F(t) |u_\alpha(t)\rangle = \epsilon_\alpha |u_\alpha(t)\rangle. \quad (\text{A4})$$

Since the Floquet functions have the property of being periodic in T , it is convenient to apply a Fourier expansion

$$|u_\alpha(t)\rangle = \sum_{n=-\infty}^{\infty} |u_\alpha^n\rangle e^{-in\Omega t}. \quad (\text{A5})$$

Doing the same for $\mathcal{H}(t)$,

$$\mathcal{H}_n = \frac{1}{T} \int_0^T dt \mathcal{H}(t) e^{in\Omega t}, \quad (\text{A6})$$

allows one to rewrite the eigenvalue problem in Eq. (A4) as

$$\sum_{m=-\infty}^{\infty} \underbrace{(\mathcal{H}_{n-m} - n\hbar\Omega\delta_{nm})}_{=:(\mathcal{H}_F)_{nm}} |u_\alpha^m\rangle = \epsilon_\alpha |u_\alpha^n\rangle. \quad (\text{A7})$$

Going to Nambu space with

$$\Psi_{\mathbf{k}}^\dagger = (\psi_{\mathbf{k}\uparrow}^\dagger, \psi_{\mathbf{k}\downarrow}^\dagger, \psi_{-\mathbf{k}\uparrow}, \psi_{-\mathbf{k}\downarrow}), \quad (\text{A8})$$

the Hamiltonian Eq. (A1) assumes the form

$$\mathcal{H}(t) = \frac{1}{2} \int d^2k \Psi_{\mathbf{k}}^\dagger (H_0(\mathbf{k}) + H_\Delta + H_1(t)) \Psi_{\mathbf{k}}, \quad (\text{A9})$$

where $\mathcal{H}_{\text{BdG}}(t) := H_0(\mathbf{k}) + H_\Delta + H_1(t)$ is a periodic BdG Hamiltonian. The static part, see Eq. (10), is given by

$$H_0 + H_\Delta = \left(\frac{\hbar^2 k^2}{2m^*} - \mu \right) \tau_z \otimes \mathbb{1}_2 + \alpha_y k_y \mathbb{1}_2 \otimes \sigma_x - \alpha_x k_x \tau_z \otimes \sigma_y + \Delta \tau_y \otimes \sigma_y, \quad (\text{A10})$$

and the driving term of general (co-) sinusoidal behavior writes as

$$H_1(t) = \begin{pmatrix} h_1(t) & \mathbf{0}_{2 \times 2} \\ \mathbf{0}_{2 \times 2} & -h_1^*(t) \end{pmatrix}. \quad (\text{A11})$$

We consider the general form $h_1(t) = \mathbf{A}(t) \cdot \boldsymbol{\sigma}$ for the time dependent driving, with

$$\mathbf{A}(t) = \mathbf{q} \cos(\Omega t) + \mathbf{r} \sin(\Omega t) \quad (\text{A12})$$

$$= \left(\frac{\mathbf{q} - i\mathbf{r}}{2} \right) e^{i\Omega t} + \left(\frac{\mathbf{q} + i\mathbf{r}}{2} \right) e^{-i\Omega t}, \quad (\text{A13})$$

which is periodic in time with a period $T = 2\pi/\Omega$ and has parameters $r_l, q_l \in \mathbb{R}$, $l \in \{x, y, z\}$. The crucial part lies now in writing down the BdG Hamiltonian in Sambe space. Here, one should keep in mind that annihilation and creation operators are adjoints of each other and should be Fourier expanded consistently. Thus,

$$\psi_{\mathbf{k}\sigma}(t) = \sum_{n=-\infty}^{\infty} e^{-in\Omega t} \psi_{\mathbf{k}\sigma, n}, \quad \psi_{\mathbf{k}\sigma}^\dagger(t) = \sum_{n=-\infty}^{\infty} e^{in\Omega t} \psi_{\mathbf{k}\sigma, n}^\dagger, \quad (\text{A14})$$

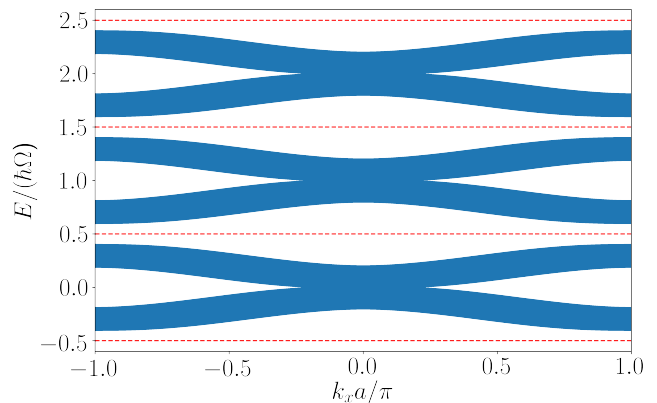


Figure 5. As expected from a Floquet Hamiltonian, replicas appear which are separated by the horizontal red dashed lines.

in the Nambu spinor. Including such time dependence has the consequence that the superconducting term parametrized by Δ couples Fourier modes n and $-n$ in the Floquet equation to be discussed below. The correct anti-diagonal position of the superconducting gap is crucial for the quasienergy spectrum to exhibit the usual appearance of replica, which we will explicitly show for the stripe geometry, Fig. 5. To be more precise, in the Nambu-Sambe basis $(\dots, \Psi_{\mathbf{k}, -N}^\dagger, \Psi_{\mathbf{k}, -N+1}^\dagger, \dots, \Psi_{\mathbf{k}, N}^\dagger, \dots)$ we find the Floquet-BdG matrix

$$(H_F)_{mn} = H_{mn} - n\delta_{mn}\hbar\Omega\tau_z \otimes \mathbb{1}_2. \quad (\text{A15})$$

In the following H_F is written down in a truncated form with N Floquet modes,

$$\begin{aligned}
H_F = & \begin{pmatrix} H_0 + N\hbar\Omega \tau_z \otimes \mathbb{1}_2 & d & \mathbf{0}_{4 \times 4} & \cdots & \mathbf{0}_{4 \times 4} \\ d^\dagger & H_0 + (N-1)\hbar\Omega \tau_z \otimes \mathbb{1}_2 & d & \cdots & \mathbf{0}_{4 \times 4} \\ & \ddots & \ddots & \ddots & \\ \mathbf{0}_{4 \times 4} & \cdots & d^\dagger & H_0 - (N-1)\hbar\Omega \tau_z \otimes \mathbb{1}_2 & d \\ \mathbf{0}_{4 \times 4} & \cdots & \mathbf{0}_{4 \times 4} & d^\dagger & H_0 - N\hbar\Omega \tau_z \otimes \mathbb{1}_2 \end{pmatrix} \\
& + \Delta \begin{pmatrix} & & & & s \\ & & & & \vdots \\ & & & & s \end{pmatrix}, \tag{A16}
\end{aligned}$$

with the matrices

$$d = \begin{pmatrix} h_1^1 & 0 \\ 0 & -(h_1^1)^* \end{pmatrix}, \tag{A17}$$

$$h_1^1 = \frac{1}{2}(\mathbf{q} - i\mathbf{r}) \cdot \boldsymbol{\sigma} \tag{A18}$$

$$= \frac{1}{2} \begin{pmatrix} q_z - ir_z & q_x - ir_x - iq_y - r_y \\ q_x - ir_x + iq_y + r_y & -q_z + ir_z \end{pmatrix}, \tag{A19}$$

$$s = \tau_y \otimes \sigma_y = \begin{pmatrix} 0 & 0 & 0 & -1 \\ 0 & 0 & 1 & 0 \\ 0 & 1 & 0 & 0 \\ -1 & 0 & 0 & 0 \end{pmatrix}. \tag{A20}$$

Here, the h_1^n are the Fourier components of $h_1(t) = h_1(t+T)$ with

$$h_1(t) = A_x(t)\sigma_x + A_y(t)\sigma_y + A_z(t)\sigma_z = \sum_{n=-\infty}^{\infty} e^{-in\Omega t} h_1^n. \tag{A21}$$

2. Löwdin high-frequency partitioning

For a general number of Floquet modes N , this truncated Floquet-BdG Hamiltonian can be only treated numerically. However, in the off-resonant regime, i.e., when the driving energy $\hbar\Omega$ exceeds the band width W , one can derive an effective BdG Hamiltonian by folding down

higher replica onto the central mode. The suitable tool to accomplish this is Löwdin partitioning which is described in great detail in [19 and 20]. In short: Assume that a Hamiltonian \mathcal{H} can be expressed as a sum of a Hamiltonian \mathcal{H}^0 with known eigenvalues E_n and eigenfunctions $|\psi_n\rangle$ and \mathcal{H}' . The latter Hamiltonian is treated as a perturbation. Decompose \mathcal{H}' further as a sum of a block diagonal matrix \mathcal{H}^1 , with subsets A and B , and \mathcal{H}^2 . Thus, we can write

$$\mathcal{H} = \mathcal{H}^0 + \mathcal{H}' = \mathcal{H}^0 + \mathcal{H}^1 + \mathcal{H}^2. \tag{A22}$$

The goal is to approximate the system consisting of block A , B and their couplings with an effective block A where the effect of block B has been “folded onto it”. Following^{19,20}, we define the indices m, m', m'' which correspond to the states in set A , and the indices l, l', l'' to the one of set B . The subsets A and B may have degeneracies but it is crucial that $E_m \neq E_l$. The matrix elements are defined by

$$\mathcal{H}'_{ij} := \langle \psi_i | \mathcal{H}' | \psi_j \rangle. \tag{A23}$$

It can be shown that a non-block-diagonal, anti-Hermitian matrix S exists which transforms \mathcal{H} into a block diagonal Hamiltonian $\tilde{\mathcal{H}} = e^{-S}\mathcal{H}e^S$, i.e., matrix S removes the coupling between block A and B . This anti-Hermitian matrix can be approximated in a successive manner which allows for an approximation of $\tilde{\mathcal{H}}$,

$$\tilde{\mathcal{H}} = \mathcal{H}^{(0)} + \mathcal{H}^{(1)} + \mathcal{H}^{(2)} + \mathcal{H}^{(3)} + \dots \tag{A24}$$

The corresponding terms with indices belonging to the block A are given by

$$\mathcal{H}_{mm'}^{(0)} = \mathcal{H}_{mm'}^0, \quad (\text{A25})$$

$$\mathcal{H}_{mm'}^{(1)} = \mathcal{H}'_{mm'}, \quad (\text{A26})$$

$$\mathcal{H}_{mm'}^{(2)} = \frac{1}{2} \sum_l \mathcal{H}'_{ml} \mathcal{H}'_{lm'} \left[\frac{1}{E_m - E_l} + \frac{1}{E_{m'} - E_l} \right], \quad (\text{A27})$$

$$\begin{aligned} \mathcal{H}_{mm'}^{(3)} = & -\frac{1}{2} \sum_{l,m''} \left[\frac{\mathcal{H}'_{ml} \mathcal{H}'_{lm''} \mathcal{H}'_{m''m'}}{(E_{m'} - E_l)(E_{m''} - E_l)} + \frac{\mathcal{H}'_{mm''} \mathcal{H}'_{m''l} \mathcal{H}'_{lm'}}{(E_m - E_l)(E_{m''} - E_l)} \right] \\ & + \frac{1}{2} \sum_{l,l'} \mathcal{H}'_{ml} \mathcal{H}'_{ll'} \mathcal{H}'_{l'm'} \left[\frac{1}{(E_m - E_l)(E_m - E_{l'})} + \frac{1}{(E_{m'} - E_l)(E_{m'} - E_{l'})} \right]. \end{aligned} \quad (\text{A28})$$

In the following we apply the Löwdin partitioning to the Floquet-BdG matrix (A16). We start by only taking the central, $n = 0$, and the $n = \pm 1$ Floquet modes into account. Thereby, we fold the $n = \pm 1$ Floquet blocks onto the central one. The Löwdin correction up to first order in $W/\hbar\Omega$, W the bandwidth, is then given by

$$\begin{aligned} H_F^{(2)} = & \frac{1}{\hbar\Omega} \begin{pmatrix} [h_1^{-1}, h_1^1] & \mathbf{0}_{2 \times 2} \\ \mathbf{0}_{2 \times 2} & -[h_1^{-1}, h_1^1]^* \end{pmatrix} \\ = & \frac{q_y r_x - q_x r_y}{\hbar\Omega} \tau_z \otimes \sigma_z + \frac{q_x r_z - q_z r_x}{\hbar\Omega} \mathbb{1}_2 \otimes \sigma_y \\ & + \frac{q_z r_y - q_y r_z}{\hbar\Omega} \tau_z \otimes \sigma_x. \end{aligned} \quad (\text{A29})$$

The second order correction is given by

$$H_F^{(3)} = C_{01} \mathbb{1}_2 \otimes \sigma_x + C_{32} \tau_z \otimes \sigma_y + C_{03} \mathbb{1}_2 \otimes \sigma_z \quad (\text{A30})$$

with

$$C_{01} = -\frac{1}{\hbar^2 \Omega^2} \mathbf{k} \cdot \begin{pmatrix} \alpha_x (q_x q_y + r_x r_y) \\ \alpha_y (q_y^2 + q_z^2 + r_y^2 + r_z^2) \end{pmatrix}, \quad (\text{A31})$$

$$C_{32} = \frac{1}{\hbar^2 \Omega^2} \mathbf{k} \cdot \begin{pmatrix} \alpha_x (q_x^2 + q_z^2 + r_x^2 + r_z^2) \\ \alpha_y (q_x q_y + r_x r_y) \end{pmatrix}, \quad (\text{A32})$$

$$C_{03} = \frac{1}{\hbar^2 \Omega^2} \mathbf{k} \cdot \begin{pmatrix} -\alpha_x (q_y q_z + r_y r_z) \\ \alpha_y (q_x q_z + r_x r_z) \end{pmatrix}. \quad (\text{A33})$$

The terms with the coefficients C_{01} and C_{32} renormalize the parts in H_0 which are due to SOC. The new term proportional to $\mathbb{1}_2 \otimes \sigma_z$ vanishes in case of an in-plane magnetic field. In the following we neglect the second order correction, leaving us with the effective 4×4 BdG Floquet Hamiltonian

$$H_{\text{eff},Z} = H_F^{(0)} + H_F^{(2)}. \quad (\text{A34})$$

3. Spectrum of the effective Hamiltonian

If the driving consists of an in plane magnetic field only the term proportional to $\tau_z \otimes \sigma_z$ survives in $H_{\text{eff},Z}$. Then we can diagonalize the spectrum in an easy way, i.e., without explicitly using Ferrari's, Descartes' or Euler's solution for quartic functions. Assuming this parameter setting, the effective static Hamiltonian has the following form

$$H_{\text{eff},Z} = \begin{pmatrix} \frac{\hbar^2 k^2}{2m^*} - \mu + h_Z & \alpha_y k_y + i\alpha_x k_x & 0 & -\Delta \\ \alpha_y k_y - i\alpha_x k_x & \frac{\hbar^2 k^2}{2m^*} - \mu - h_Z & \Delta & 0 \\ 0 & \Delta & -\frac{\hbar^2 k^2}{2m^*} + \mu - h_Z & \alpha_y k_y - i\alpha_x k_x \\ -\Delta & 0 & \alpha_y k_y + i\alpha_x k_x & -\frac{\hbar^2 k^2}{2m^*} + \mu + h_Z \end{pmatrix} \quad (\text{A35})$$

where h_Z , which appears due to the effective field, Eq. (A29), is given by

$$h_Z := \frac{\Lambda_z}{\hbar\Omega} = \frac{q_y r_x - q_x r_y}{\hbar\Omega}. \quad (\text{A36})$$

The diagonal 2×2 -blocks are diagonalized by the matrix

$$V_1(\mathbf{k}) = \begin{pmatrix} v_1(\mathbf{k}) & \mathbf{0}_{2 \times 2} \\ \mathbf{0}_{2 \times 2} & v_2(\mathbf{k}) \end{pmatrix} \quad (\text{A37})$$

where

$$v_1(\mathbf{k}) = \begin{pmatrix} \gamma_+(\mathbf{k}) & -\gamma_-(\mathbf{k})e^{-i\varphi(\mathbf{k})} \\ \gamma_-(\mathbf{k})e^{i\varphi(\mathbf{k})} & \gamma_+(\mathbf{k}) \end{pmatrix}, \quad (\text{A38})$$

$$v_2(\mathbf{k}) = \begin{pmatrix} \gamma_-(\mathbf{k})e^{i\varphi(\mathbf{k})} & \gamma_+(\mathbf{k}) \\ \gamma_+(\mathbf{k}) & -\gamma_-(\mathbf{k})e^{-i\varphi(\mathbf{k})} \end{pmatrix} \quad (\text{A39})$$

with

$$\gamma_{\pm}(\mathbf{k}) = \sqrt{\frac{1}{2} \left(1 \pm \frac{h_Z}{\sqrt{(\alpha_x k_x)^2 + (\alpha_y k_y)^2 + h_Z^2}} \right)}, \quad (\text{A40})$$

and

$$e^{i\varphi(\mathbf{k})} = \frac{\alpha_y k_y - i\alpha_x k_x}{\sqrt{(\alpha_y k_y)^2 + (\alpha_x k_x)^2}}. \quad (\text{A41})$$

The Hamiltonian (A35) is rendered as

$$V_1^\dagger H V_1 = \begin{pmatrix} \eta_+ & 0 & -\Delta_2 & \Delta_1^* \\ 0 & \eta_- & \Delta_1 & \Delta_2 \\ -\Delta_2 & \Delta_1^* & -\eta_- & 0 \\ \Delta_1 & \Delta_2 & 0 & -\eta_+ \end{pmatrix} \quad (\text{A42})$$

where now

$$\eta_{\pm}(\mathbf{k}) = \frac{\hbar^2 k^2}{2m^*} - \mu \pm \sqrt{(\alpha_x k_x)^2 + (\alpha_y k_y)^2 + h_Z^2}. \quad (\text{A43})$$

Explicitly, we find that

$$\Delta_1 = 2\Delta\gamma_+\gamma_-e^{i\varphi}, \quad \Delta_2 = \Delta(\gamma_+^2 - \gamma_-^2), \quad (\text{A44})$$

and hence the intraband pairing Δ_1 is an odd function in the wave vector \mathbf{k} . In contrast, the interband pairing Δ_2 is an even function of momentum. The transformed Hamiltonian Eq. (A42) thus reveals the presence of an effective p -wave intravalley pairing, a necessary requirement for topological superconductivity⁷. To fully uncover the topological properties of the effective Hamiltonian, we now follow Ref. 45 and apply the transformation

$$V_2 = \begin{pmatrix} \delta_+ & 0 & \delta_- & 0 \\ 0 & \delta_- & 0 & \delta_+ \\ -\delta_- & 0 & \delta_+ & 0 \\ 0 & -\delta_+ & 0 & \delta_- \end{pmatrix} \quad (\text{A45})$$

with

$$\delta_{\pm} = \sqrt{\frac{1}{2} \left(1 \pm \frac{(\eta_+ + \eta_-)/2}{\sqrt{(\eta_+ + \eta_-)^2/4 + \Delta_2^2}} \right)}. \quad (\text{A46})$$

This transformation results in

$$V_2^\dagger V_1^\dagger H V_1 V_2 = \begin{pmatrix} \lambda_+ & -\Delta_1^* & 0 & 0 \\ -\Delta_1 & -\lambda_+ & 0 & 0 \\ 0 & 0 & \lambda_- & \Delta_1^* \\ 0 & 0 & \Delta_1 & -\lambda_- \end{pmatrix} \quad (\text{A47})$$

where

$$\lambda_{\pm} = \frac{\eta_+ - \eta_-}{2} \pm \sqrt{\frac{(\eta_+ + \eta_-)^2}{4} + \Delta_2^2}. \quad (\text{A48})$$

Finally we can diagonalize the remaining 2×2 matrices. The four eigenvalues are given by

$$\lambda_{mn} = m(\hbar_{Z,c}^2 + h_Z^2 + \bar{k}^2(\bar{\alpha}^2 + \bar{\beta}^2 - 2\xi\mu + 2\bar{\alpha}\bar{\beta}\cos(2\theta)) + \xi^2\bar{k}^4 + 2n\sqrt{\mathcal{W}})^{\frac{1}{2}} \quad (\text{A49})$$

with $m = \pm 1$, $n = \pm 1$ and the critical field

$$|h_{Z,c}| = \sqrt{\Delta^2 + \mu^2}. \quad (\text{A50})$$

We introduced the abbreviation

$$\begin{aligned} \mathcal{W} := & \hbar_{Z,c}^2 h_Z^2 + \bar{k}^2 \mu (\bar{\alpha}^2 + \bar{\beta}^2) \mu - 2\hbar_{Z,c}^2 \xi + 2\bar{\alpha}\bar{\beta}\mu \cos(2\theta) \\ & + \bar{k}^4 \xi (h_Z^2 \xi - 2(\bar{\alpha}^2 + \bar{\beta}^2) \mu - 4\bar{\alpha}\bar{\beta}\mu \cos(2\theta)) \\ & + \bar{k}^6 \xi^2 (\bar{\alpha}^2 + \bar{\beta}^2 + 2\bar{\alpha}\bar{\beta}\cos(2\theta)), \end{aligned} \quad (\text{A51})$$

where we used polar coordinates with $\bar{k}_x = \bar{k} \cos(\theta)$, $\bar{k}_y = \bar{k} \sin(\theta)$, and defined dimensionless quantities $\bar{k} := ka$, $\bar{\alpha} := \alpha/a$, $\bar{\beta} := \beta/a$, with a the lattice constant. Finally, $\xi := \hbar^2/(2m^*a^2)$ is the hopping energy.

Appendix B: Floquet BdG Hamiltonian in the tight-binding formulation

1. Tight-binding version of the static Hamiltonian

For many numerical purposes it is convenient to work with a tight-binding Hamiltonian which reduces to the static Hamiltonian Eq. (2) in the long wave length limit. Working on a square lattice with spacing a , the latter quantity is reformulated as

$$\begin{aligned} \mathcal{H}_0 + \mathcal{H}_\Delta = & \sum_{ml\sigma} \left[(4\xi - \mu) c_{ml\sigma}^\dagger c_{ml\sigma} - \xi (c_{(m+1)l\sigma}^\dagger c_{ml\sigma} \right. \\ & \left. + c_{m(l+1)\sigma}^\dagger c_{ml\sigma} + \text{H.c.}) \right] \\ & + \sum_{ml} \left[-\frac{\bar{\alpha}_x}{2} (c_{(m+1)l\uparrow}^\dagger c_{ml\downarrow} - c_{ml\uparrow}^\dagger c_{(m+1)l\downarrow} + \text{H.c.}) \right. \\ & \left. + i\frac{\bar{\alpha}_y}{2} (c_{m(l+1)\uparrow}^\dagger c_{ml\downarrow} - c_{ml\uparrow}^\dagger c_{m(l+1)\downarrow} - \text{H.c.}) \right] \\ & - \frac{\Delta}{2} \sum_{ml} (c_{ml\uparrow}^\dagger c_{ml\downarrow}^\dagger - c_{ml\downarrow}^\dagger c_{ml\uparrow}^\dagger + \text{H.c.}), \end{aligned} \quad (\text{B1})$$

where the operators $c_{ml\sigma}^\dagger$, $c_{ml\sigma}$ create and annihilate, respectively, a particle with spin $\sigma \in \{\uparrow, \downarrow\}$ at lattice site $\mathbf{r} = ma \mathbf{e}_x + la \mathbf{e}_y$. We have redefined the spin-orbit parameters as $\bar{\alpha}_x := \alpha_x/a$, $\bar{\alpha}_y := \alpha_y/a$.

Let us now concentrate on an infinite stripe along the y -direction with L transversal lattice sites numbered by $m \in \{0, \dots, L-1\}$. Introducing the operators

$$c_{m\sigma}^\dagger(k) = \sqrt{\frac{a}{2\pi}} \sum_l e^{ikal} c_{ml\sigma}^\dagger \quad (\text{B2})$$

for each wave number $k \in [-\pi/a, \pi/a]$ along with the Nambu spinor

$$\Psi_q^\dagger(k) = (\phi_0^\dagger(k), \dots, \phi_{L-1}^\dagger(k)), \quad q \in \{0, \dots, 4L-1\}, \quad (\text{B3})$$

where

$$\phi_m^\dagger(k) = (c_{m\uparrow}^\dagger(k), c_{m\downarrow}^\dagger(k), c_{m\uparrow}^\dagger(-k), c_{m\downarrow}^\dagger(-k)), \quad (\text{B4})$$

the static Hamiltonian can be expressed as

$$\mathcal{H}_0 + \mathcal{H}_\Delta = \frac{1}{2} \int_{-\pi/a}^{\pi/a} dk \sum_{q,q'=0}^{4L-1} \Psi_q^\dagger(k) H_{qq'}(k) \Psi_{q'}(k). \quad (\text{B5})$$

Here the BdG Hamiltonian in stripe geometry reads

$$H_{qq'}(k) = \begin{pmatrix} a(k) & b & & & \\ b^\dagger & a(k) & b & & \\ & b^\dagger & a(k) & b & \\ & & \ddots & \ddots & \ddots \end{pmatrix}, \quad (\text{B6})$$

with

$$a(k) = \begin{pmatrix} \eta(k) & \bar{\alpha}_y \sin(ka) & 0 & -\Delta \\ \bar{\alpha}_y \sin(ka) & \eta(k) & \Delta & 0 \\ 0 & \Delta & -\eta(k) & \bar{\alpha}_y \sin(ka) \\ -\Delta & 0 & \bar{\alpha}_y \sin(ka) & -\eta(k) \end{pmatrix}, \quad (\text{B7})$$

$$\eta(k) = (4 - 2 \cos(ka))\xi - \mu, \quad (\text{B8})$$

and

$$b = \begin{pmatrix} -\xi & \bar{\alpha}_x/2 & 0 & 0 \\ -\bar{\alpha}_x/2 & -\xi & 0 & 0 \\ 0 & 0 & \xi & -\bar{\alpha}_x/2 \\ 0 & 0 & \bar{\alpha}_x/2 & \xi \end{pmatrix}. \quad (\text{B9})$$

Note that the matrix (B6) is real and symmetric.

For a stripe along the x -direction with again L transversal lattice sites numbered now by $l \in \{0, \dots, L-1\}$ one defines operators

$$c_{l\sigma}^\dagger(k) = \sqrt{\frac{a}{2\pi}} \sum_m e^{ikam} c_{ml\sigma}^\dagger, \quad (\text{B10})$$

and the entries of the spinor (B3) now read

$$\phi_m^\dagger(k) = (c_{l\uparrow}^\dagger(k), c_{l\downarrow}^\dagger(k), c_{l\uparrow}^\dagger(-k), c_{l\downarrow}^\dagger(-k)). \quad (\text{B11})$$

The resulting BdG matrix is again of the form (B6) where now

$$a(k) = \begin{pmatrix} \eta(k) & i\bar{\alpha}_x \sin(ka) & 0 & -\Delta \\ -i\bar{\alpha}_x \sin(ka) & \eta(k) & \Delta & 0 \\ 0 & \Delta & -\eta(k) & -i\bar{\alpha}_x \sin(ka) \\ -\Delta & 0 & i\bar{\alpha}_x \sin(ka) & -\eta(k) \end{pmatrix}, \quad (\text{B12})$$

$$b = \begin{pmatrix} -\xi & -i\bar{\alpha}_y/2 & 0 & 0 \\ -i\bar{\alpha}_y/2 & -\xi & 0 & 0 \\ 0 & 0 & \xi & -i\bar{\alpha}_y/2 \\ 0 & 0 & -i\bar{\alpha}_y/2 & \xi \end{pmatrix}. \quad (\text{B13})$$

2. Tight-binding Floquet-BdG Hamiltonian in Nambu-Sambe space

Again, we consider the same driving as in Eq. (A11). Taking into account $2N+1$ Fourier modes with labels $n \in \{-N, -N+1, \dots, N\}$ around the central temporal Brillouin zone, the Nambu-Sambe spinor has $4L(2N+1)$ components. The Floquet-BdG Hamiltonian takes the form

$$H_F(k) = H_{\text{btd}}(k) + H_\Delta, \quad (\text{B14})$$

where the first contribution is block-tridiagonal,

$$H_{\text{btd}}(k) = \begin{pmatrix} H(k) + N\hbar\Omega T^z & & & & \\ & D^+ & & & \\ & & H(k) + (N-1)\hbar\Omega T^z & & D \\ & & & \ddots & \ddots \\ & & & & D \\ & & & & & D^+ & H(k) - N\hbar\Omega T^z \end{pmatrix} \quad (\text{B15})$$

with $H(k)$ being the $4L \times 4L$ BdG matrix (B6), but now without the superconducting coupling so that its diagonal blocks read

$$a(k) = \begin{pmatrix} \eta(k) & \bar{\alpha}_y \sin(ka) & 0 & 0 \\ \bar{\alpha}_y \sin(ka) & \eta(k) & 0 & 0 \\ 0 & 0 & -\eta(k) & \bar{\alpha}_y \sin(ka) \\ 0 & 0 & \bar{\alpha}_y \sin(ka) & -\eta(k) \end{pmatrix}. \quad (\text{B16})$$

The matrix T^z is diagonal,

$$T^z = \begin{pmatrix} \tau^z \otimes \mathbb{1}_2 & & & \\ & \tau^z \otimes \mathbb{1}_2 & & \\ & & \ddots & \\ & & & \tau^z \otimes \mathbb{1}_2 \end{pmatrix}. \quad (\text{B17})$$

The driving is further implemented in the block-diagonal matrix

$$D = \begin{pmatrix} d & & & \\ & d & & \\ & & \ddots & \\ & & & d \end{pmatrix}, \quad (\text{B18})$$

with d defined in Eq. (A17). Finally, the superconducting coupling is included in the contribution

$$H_\Delta = \begin{pmatrix} & & & S \\ & & & \\ & & \ddots & \\ S & S & & \end{pmatrix} \quad (\text{B19})$$

where the $4L \times 4L$ matrix S is given by

$$S = \begin{pmatrix} s & & & \\ & s & & \\ & & \ddots & \\ & & & s \end{pmatrix}, \quad (\text{B20})$$

with s defined in Eq. (A20).

As mentioned in Sec. A1, the correct anti-diagonal position of the superconducting gap Δ in the Floquet space, connecting the n with the $-n$ Floquet mode, results in a quasienergy spectrum which shows the usual appearance of replica. The spectrum of the Floquet Hamiltonian in stripe geometry is shown in Fig. 5. We show the central Floquet band and the two Floquet replicas above it.

3. Tight-binding spectra and Chern numbers

To determine from the 2D spectrum whether or not we can find topologically protected boundary modes in a stripe geometry, we calculate the Chern numbers C_α for the bulk system. The latter are determined by integrating over the Berry curvature $\mathbf{F}_\alpha(\mathbf{k})$ ^{29–31},

$$C_\alpha = \frac{1}{2\pi} \int_{\text{BZ}} d^2k \mathbf{F}_\alpha(\mathbf{k}) \cdot \hat{\mathbf{z}}, \quad (\text{B21})$$

with

$$\mathbf{F}_\alpha(\mathbf{k}) = \sum_{\beta \neq \alpha} \text{Im} \frac{\langle u_{\mathbf{k}\alpha}^n | \nabla_{\mathbf{k}} H_F | u_{\mathbf{k}\beta}^n \rangle \times \langle u_{\mathbf{k}\beta}^n | \nabla_{\mathbf{k}} H_F | u_{\mathbf{k}\alpha}^n \rangle}{(\varepsilon_{\mathbf{k}\alpha} - \varepsilon_{\mathbf{k}\beta})^2}. \quad (\text{B22})$$

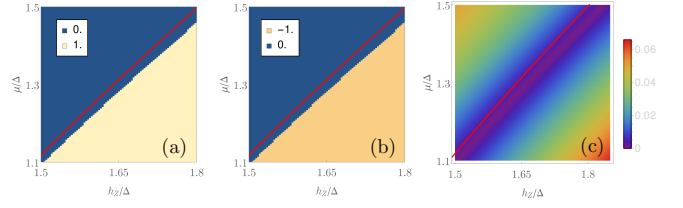


Figure 6. Chern numbers of the second (a) and third (b) band of the first Floquet Brillouin zone of H_F . (c) Energy gap between the second and third band of the central Floquet mode of H_F in units of ξ . Values are calculated using the tight-binding formulation and shown for different field strengths h_Z and chemical potential μ in units of the superconducting gap Δ . The red line indicates $|h_{Z,c}|$, Eq. (A50). Parameters used: $N_F = 5$ and the frequency is $\hbar\Omega/\xi = 20$, $q_x = q_y = 0$, $r_z = 1$ ξ , $\alpha = 0.1$ ξa , $\beta = 0.37$ ξa .

The $|u_{\mathbf{k}\alpha}^n\rangle$, $\alpha = 1, 2, 3, 4$, are the eigenstates of the n -th Floquet mode of the Floquet-BdG tight-binding Hamiltonian. In Figs. 6(a) and 6(b) we also show the Chern number of the second and third Floquet bands ($\alpha = 2, 3$) within the first Floquet Brillouin zone ($n = 0$). We restricted to a smaller range of chemical potentials compared to Fig. 2. In this way we notice a small difference between the phase boundary as evinced from the numerically calculated Chern numbers, and the one obtained from the effective continuum Hamiltonian, Eq. (A50), given by the solid red line. This difference is due to the fact that the gap closing condition is slightly shifted compared to the tight-binding model, as shown in Fig. 6(c).

Finally, we show in Fig. 7 energy gaps for a lower driving frequency $\hbar\Omega = 16\xi$. In Fig. 7(a) the smallest energy gap between the bands of the central Floquet mode is shown on a larger parameter scale with the red line indicating the analytically found phase boundary. As one can see from Fig. 7(b), which shows the smallest energy gap between different Floquet replica, for the largest part of the parameter space the driving frequency is too low to be in the off-resonant regime. The dashed line indicates the parameters where the modes from two different replica touch.

Appendix C: Characterization of the topological phase and edge states

We are going to discuss different conditions for the Rashba and Dresselhaus SOC parameters. The ratio between both controls the appearance of flat bands. From Eq. (A49), we can extract the field h_Z at which the central gap closes. One finds the following four conditions,

$$h_{Z,mn}(\bar{k}) = m \sqrt{\xi^2 \bar{k}^4 + h_{Z,c}^2 + n \sqrt{-2\bar{k}^2 \Delta^2 \gamma - \frac{\bar{k}^2}{2}(4\xi\mu + \gamma)}}, \quad (\text{C1})$$

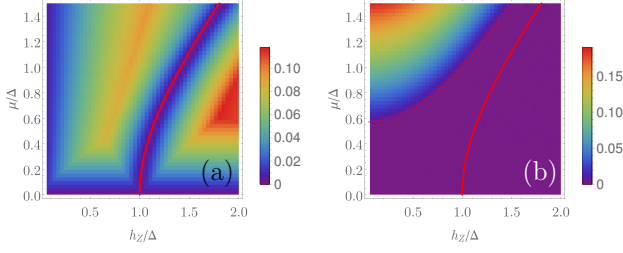


Figure 7. Smallest energy gap in units of ξ . (a) Shown is the gap between the second and third band of the central Floquet mode of H_F . (b) Smallest energy gap between different Floquet replica, of H_F for different values of field strength h_Z and chemical potential μ . Parameters used: $N_F = 5$ and the frequency is $\hbar\Omega/\xi = 16$, $q_x = q_z = 0$, $r_z = 1 \xi$, $\alpha = 0.1 \xi a$, $\beta = 0.37 \xi a$.

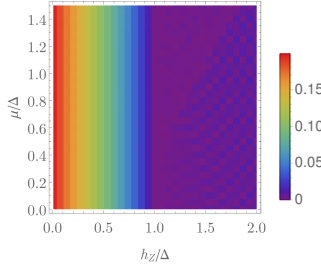


Figure 8. Central gap of the 2D Floquet spectrum in units of ξ for $\alpha = \beta$. The gap closes for $h_Z = \sqrt{\Delta^2 + \mu^2}$ at $k = 0$. However, there is already a gap closing at finite wave vectors for $h_Z \geq \Delta$, see discussion in Sec. C2. The parameters are $\alpha = \beta = 0.37 \xi a$, $N_F = 3$, $\Delta = 0.1 \xi$, $r_x = 1 \xi$, $r_y = 0.2 \xi$, $r_z = q_x = q_y = 0$.

with $m = \pm 1$, $n = \pm 1$ and

$$\gamma := 2(\bar{\alpha}^2 + \bar{\beta}^2 + 2\bar{\alpha}\bar{\beta}\cos(2\theta)). \quad (\text{C2})$$

We distinguish three cases:

1. $|\alpha| \neq |\beta|$

A gap closing only happens for $\bar{k} = 0$; thus one ends up with the critical fields $h_{Z,\pm,n}(\bar{k} = 0) \equiv h_{Z\pm}(\bar{k} = 0) := \pm h_{Z,c} = \pm \sqrt{\Delta^2 + \mu^2}$. An example for the $|\alpha| \neq |\beta|$ condition is shown in Fig. 2. This case can be well understood in terms of Chern numbers.

As one can see, the gap closing at $\bar{k} = 0$ does not depend on the SOC. However, in the following it will be shown that a gap also closes at a finite momentum $\bar{k} = \sqrt{\mu/\xi}$ if $|\alpha| = |\beta|$. The needed critical field in this case is equal or smaller than $h_{Z,c}$. Let us first consider the case $\alpha = \beta$.

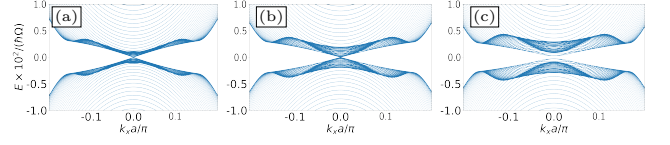


Figure 9. Quasienergy spectrum of $H_F(k)$ in stripe geometry with a width of $N_y = 200$ transverse channels and for SOC parameters $\alpha = \beta$. The three panels show different field strengths. The field is changed via q_y (for fixed frequency $\hbar\Omega = 20 \xi$ and $N_F = 4$) for $\alpha = \beta = 0.1 \xi a$. [$\Delta = 0.1 \xi$, $\mu = 0.1 \xi$, $r_x = 2 \xi$, $r_y = 0.2 \xi$, $q_x = 0$, $h_{Z,c}/\Delta = \sqrt{2}$]: (a) $q_y = 1.2 \xi$, thus $h_Z/h_{Z,c} = 0.85$, (b) $q_y = 1.4 \xi$, thus $h_Z/h_{Z,c} = 0.99$, (c) $q_y = 1.6 \xi$, thus $h_Z/h_{Z,c} = 1.13$.

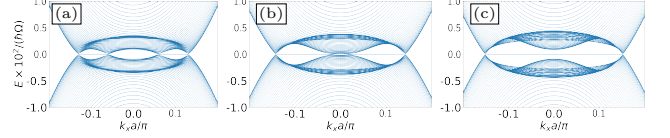


Figure 10. Quasienergy spectrum of $H_F(k)$ in stripe geometry with a width of $N_y = 200$ transverse channels and for SOC parameters $\alpha = -\beta$. The three panels show different field strengths. The field is changed via q_y (for fixed frequency $\Omega = 20 \xi$ and $N_F = 4$) for $\alpha = -\beta = 0.1 \xi a$. [$\Delta = 0.1 \xi$, $\mu = 0.1 \xi$, $r_x = 2 \xi$, $r_y = 0.2 \xi$, $q_x = 0$, $h_{Z,c}/\Delta = \sqrt{2}$]: (a) $q_y = 1.2 \xi$, thus $h_Z/h_{Z,c} = 0.85$, (b) $q_y = 1.4 \xi$, thus $h_Z/h_{Z,c} = 0.99$, (c) $q_y = 1.6 \xi$, thus $h_Z/h_{Z,c} = 1.13$.

2. $\alpha = \beta$

In this case, γ simplifies to $\gamma = 4\bar{\alpha}^2(1 + \cos(2\theta))$ and a necessary condition for a gap closing at a finite \bar{k} is $\theta = \pi/2$. In other terms, $\bar{k}_x = 0$ and $\bar{k}_y = \bar{k}$, i.e., a gap closing can be found along the y -direction in k -space. Equation (C1) yields (sign n is redundant since $\gamma = 0$)

$$h_{Z,\pm}(\bar{k}) = \pm h_{Z,c}(\bar{k}) := \sqrt{\Delta^2 + (\mu - \bar{k}^2 \xi)^2}. \quad (\text{C3})$$

Thus, the smallest field at which the gap closes is

$$|h_{Z,c}(\bar{k} = \mu/\xi)| = \Delta \leq h_{Z,c}. \quad (\text{C4})$$

Since we are free to choose k as large as we want in Eq. (C3), there is no gap re-opening if the field is enlarged, as shown in Fig. 8. This is in contrast to the $|\alpha| \neq |\beta|$ case. The quasienergy spectrum in case of a stripe geometry with confinement in the y -direction is exemplarily shown in Fig. 9 for various values of the field strength changed via q_y . As expected, for this orientation of the stripe no closing occurs.

3. $\alpha = -\beta$

Here, the only difference to the $\alpha = \beta$ case is the direction at which the gap closing happens which is $\theta = 0$. As for case C2, depending on the stripe direction, one

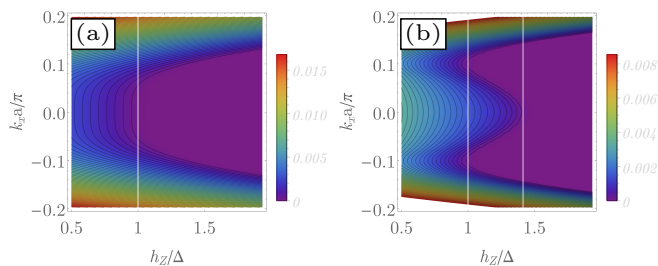


Figure 11. Central gap, in units of $\hbar\Omega$, plotted for $\alpha = -\beta = 0.1 \xi$ with (a) $\mu = 0$ and (b) $\mu = 0.1 \xi$. In (a) the vertical line indicates the critical field $h_Z/\Delta = 1$ below which one finds a gapped system. In (b) the second vertical line indicates $h_{Z,c}$. Other parameters: $N_F = 2$, $\Delta = 0.1 \xi$, $r_x = 1 \xi$, $r_y = 0.2 \xi$, $r_z = q_x = q_y = 0$.

can see either a gap-closing and re-opening if increasing the field h_Z or only a closing without gap re-opening. The energy spectrum for such a case in stripe geometry is shown in Fig. 3 and reported here also in Fig. 10. In addition, we plot in Fig. 11 the central energy gap as a function of the longitudinal wave vector and the field h_Z . Figure 11 shows nicely how the separated flat bands merge to one with increasing h_Z .

4. Partial Berry-phase

From the spectrum analysis above and especially Eq. (C3), the region where we find disconnected flat bands [Fig. 10 (a) and (b)] is given by $\Delta < h_Z < |h_{Z,c}|$. This can be understood by counting the band touchings of the two central bands (for $\mu = 0$ and $\mu = 0.1 \xi$ the

central gap is plotted in Fig. 11). From Eq. (C3) this happens at

$$\bar{k}_{\pm} = \sqrt{\frac{\mu}{\xi} \pm \frac{1}{\xi} \sqrt{h_Z^2 - \Delta^2}}. \quad (\text{C5})$$

For $h_Z \geq h_{Z,c}$, we are left with only one real value, \bar{k}_+ . Since the gap at $\bar{k} = 0$ is closed for fields h_Z larger than Δ for $|\alpha| = |\beta|$, one fails to calculate the Chern numbers of the central two bands. However, examining Fig. 10, one expects the existence of a topological quantity which distinguishes the parameter space where we find disconnected flat bands from the one where we find only one connected flat band as shown in Fig. 10 (c). To connect this change of band-touchings with a change of topology of the spectrum, we follow the method presented in Refs. [18 and 46] and calculate the “partial” topological quantum number called *partial Berry-phase sum parity* (PBSP). According to Refs. [18 and 46] we fix one of the wave vector components by $k_p \in \{0, \pi\}$, $p \in \{x, y\}$ and calculate the PBSP (in the following we choose k_x to be fixed)

$$P_B = (-1)^{\text{mod}_{2\pi}(B_{+,k_x})/\pi}, \quad B_+ = B_{k_x,1} + B_{k_x,2} \quad (\text{C6})$$

with

$$B_{k_x,n} = i \int_{-\pi}^{\pi} dk_y \langle \phi_{n,k_y} | \partial_{k_y} \phi_{n,k_y} \rangle, \quad (\text{C7})$$

where n is the index of the two negative occupied bands. The numerical evaluation of B_n , which has to guarantee numerically gauge invariance, is described in detail in Appendix D of Ref. [46]. The result for $k_x = 0$, $\alpha_x = 0$ is shown in Fig. 3(d). For $k_x = \pi/a$ one finds the same result.

* wenkp@wwu.de

¹ T. Oka and S. Kitamura, *Annual Review of Condensed Matter Physics* **10**, 387 (2019).
² J. H. Shirley, *Physical Review* **138**, B979 (1965).
³ M. Grifoni and P. Hänggi, *Physics Reports* **304**, 229 (1998).
⁴ U. Bovensiepen and P. S. Kirchmann, *Laser & Photonics Reviews* **6**, 589 (2012).
⁵ Y. H. Wang, H. Steinberg, P. Jarillo-Herrero, and N. Gedik, *Science* **342**, 453 (2013).
⁶ T. Kitagawa, T. Oka, A. Brataas, L. Fu, and E. Demler, *Physical Review B* **84**, 235108 (2011).
⁷ M. Sato and Y. Ando, *Reports on Progress in Physics* **80**, 076501 (2017).
⁸ L. Jiang, T. Kitagawa, J. Alicea, A. R. Akhmerov, D. Pekker, G. Refael, J. I. Cirac, E. Demler, M. D. Lukin, and P. Zoller, *Physical Review Letters* **106** (2011).
⁹ A. A. Reynoso and D. Frustaglia, *Physical Review B* **87**, 115420 (2013).
¹⁰ M. Thakurathi, A. A. Patel, D. Sen, and A. Dutta, *Physical Review B* **88**, 155133 (2013).

¹¹ G.-B. Liu, W.-Y. Shan, Y. Yao, W. Yao, and D. Xiao, *Physical Review B* **88**, 085433 (2013).
¹² A. Kundu and B. Seradjeh, *Physical Review Letters* **111**, 136402 (2013).
¹³ M. Thakurathi, D. Loss, and J. Klinovaja, *Physical Review B* **95**, 155407 (2017).
¹⁴ M. Thakurathi, K. Sengupta, and D. Sen, *Physical Review B* **89**, 235434 (2014).
¹⁵ A. Poudel, G. Ortiz, and L. Viola, *EPL (Europhysics Letters)* **110**, 17004 (2015).
¹⁶ K. Takasan, A. Daido, N. Kawakami, and Y. Yanase, *Physical Review B* **95**, 134508 (2017).
¹⁷ K. Plekhanov, M. Thakurathi, D. Loss, and J. Klinovaja, *Physical Review Research* **1**, 032013 (2019).
¹⁸ S. Deng, G. Ortiz, A. Poudel, and L. Viola, *Physical Review B* **89**, 140507 (2014).
¹⁹ G. L. Bir and G. E. Pikus, *Symmetry and Strain-induced Effects in Semiconductors* (Wiley, New York, 1974).
²⁰ R. Winkler, *Spin-Orbit Coupling Effects in Two-Dimensional Electron and Hole Systems*, Springer Tracts in Modern Physics, Vol. 191 (Springer Berlin Heidelberg,

- Berlin, Heidelberg, 2003) p. 228.
- ²¹ Y. Bychkov and E. I. Rashba, *JETP Lett.* **39**, 78 (1984).
 - ²² E. Rashba and Sheka, “Symmetry of Energy Bands in Crystals of Wurtzite Type II. Symmetry of Bands with Spin-Orbit Interaction Included,” <http://nrs.harvard.edu/urn-3:HUL.InstRepos:29426010> (2015).
 - ²³ G. Dresselhaus, *Physical Review* **100**, 580 (1955).
 - ²⁴ Tensor convention: $\tau_z \otimes \sigma_i = \begin{pmatrix} \sigma_i & \mathbf{0}_2 \\ \mathbf{0}_2 & -\sigma_i \end{pmatrix}$.
 - ²⁵ A. S. Sheremet, O. V. Kibis, A. V. Kavokin, and I. A. Shelykh, *Physical Review B* **93**, 165307 (2016).
 - ²⁶ D. E. Liu, A. Levchenko, and H. U. Baranger, *Physical Review Letters* **111**, 047002 (2013).
 - ²⁷ J. Alicea, *Reports on Progress in Physics* **75**, 076501 (2012).
 - ²⁸ J. D. Sau, R. M. Lutchyn, S. Tewari, and S. D. Sarma, *Physical Review Letters* **104**, 040502 (2010).
 - ²⁹ D. J. Thouless, M. Kohmoto, M. P. Nightingale, and M. Den Nijs, *Physical Review Letters* **49**, 405 (1982).
 - ³⁰ M. V. Berry, *Proceedings of the Royal Society A* **392**, 45 (1984).
 - ³¹ B. Simon, *Physical Review Letters* **51**, 2167 (1983).
 - ³² J. Schliemann, J. C. Egues, and D. Loss, *Physical Review Letters* **90**, 146801 (2003).
 - ³³ J. D. Koralek, C. P. Weber, J. Orenstein, B. A. Bernevig, S.-C. Zhang, S. Mack, and D. D. Awschalom, *Nature* **458**, 610 (2009).
 - ³⁴ M. Kammermeier, P. Wenk, and J. Schliemann, *Physical Review Letters* **117**, 236801 (2016).
 - ³⁵ J. Schliemann, *Reviews of Modern Physics* **89**, 011001 (2017).
 - ³⁶ D. Oshima, S. Ikegaya, A. P. Schnyder, and Y. Tanaka, *Phys. Rev. Research* **4**, L022051 (2022).
 - ³⁷ A. Altland and M. R. Zirnbauer, *Physical Review B* **55**, 1142 (1997).
 - ³⁸ R. V. Mishmash, D. Aasen, A. P. Higginbotham, and J. Alicea, *Physical Review B* **93**, 245404 (2016).
 - ³⁹ N. Leumer, M. Grifoni, B. Muralidharan, and M. Marganska, *Physical Review B* **103**, 165432 (2021).
 - ⁴⁰ F. Qu, J. van Veen, F. K. de Vries, A. J. A. Beukman, M. Wimmer, W. Yi, A. A. Kiselev, B.-M. Nguyen, M. Sokolich, M. J. Manfra, F. Nichele, C. M. Marcus, and L. P. Kouwenhoven, *Nano Letters* **16**, 6509 (2016).
 - ⁴¹ X. Xi, Z. Wang, W. Zhao, J.-H. Park, K. T. Law, H. Berger, L. Forró, J. Shan, and K. F. Mak, *Nature Physics* **12**, 139 (2015).
 - ⁴² M. Kuzmanović, T. Dvir, D. LeBoeuf, S. Ilić, D. Möckli, M. Haim, S. Kraemer, M. Khodas, M. Houzet, J. S. Meyer, M. Aprili, H. Steinberg, and C. H. L. Quay, “Tunneling spectroscopy of few-monolayer NbSe₂ in high magnetic field: Ising protection and triplet superconductivity,” (2021), [arXiv:2104.00328 \[cond-mat.supr-con\]](https://arxiv.org/abs/2104.00328).
 - ⁴³ T. Mikami, S. Kitamura, K. Yasuda, N. Tsuji, T. Oka, and H. Aoki, *Physical Review B* **93**, 144307 (2016).
 - ⁴⁴ G. Floquet, *Annales scientifiques de l'École normale supérieure* **12**, 47 (1883).
 - ⁴⁵ M. Marganska, L. Milz, W. Izumida, C. Strunk, and M. Grifoni, *Physical Review B* **97**, 075141 (2018).
 - ⁴⁶ S. Deng, G. Ortiz, and L. Viola, *Physical Review B* **87**, 205414 (2013).